Simulation and extended range prediction of monsoon intraseasonal oscillations in NCEP CFS/GFS version 2 framework

A. K. Sahai[1,*], S. Sharmila[1], S. Abhilash[1], R. Chattopadhyay[1], N. Borah[1], R. P. M. Krishna[1], S. Joseph[1], M. Roxy[1], S. De[1], S. Pattnaik[2] and P. A. Pillai[1]

[1]Indian Institute of Tropical Meteorology, Dr Homi Bhabha Road, Pashan, Pune 411 008, India
[2]Department of Earth, Ocean and Climate Sciences, Indian Institute of Technology, Bhubaneswar 751 013, India

The present study investigates the role of ocean–atmosphere coupling in improving the simulation and extended range prediction skill of the monsoon intraseasonal oscillations (MISOs) using the NCEP CFS (version 2) vis-à-vis its atmospheric component GFS (version 2) forced with bias-corrected sea-surface temperature (SST) derived from CFS. Though the CFS free-run analysis shows dry bias over Indian land as compared to GFS, the interactive air–sea coupling in CFS has considerably improved the simulation of large-scale dynamical fields, SST–rainfall relationship, and the northward propagation of the MISOs with respect to GFS. However, the improvement of MISO simulation in CFS over GFS has not necessarily guaranteed the improvement of real-time extended range prediction during 2011 and 2012. CFS shows better skill over GFS (forced with bias-corrected CFS derived SST) at pentad lead 4. The phases of MISOs are better predicted in GFS and the amplitude prediction skill is marginally improved in CFS. The present study also advocates the need of probabilistic category (active, normal or break) forecast at extended range.

Keywords: Air–sea interaction, extended range prediction, monsoon intraseasonal oscillations, ocean–atmosphere coupling, sea surface temperature.

Introduction

THE extended range prediction (ERP) of the boreal summer monsoon intraseasonal oscillations (MISO) and the daily rainfall of Indian summer monsoon (ISM) have been attempted in various studies in the past as well as in recent times using statistical[1–5] and dynamical models[6–13]. With the recent adoption of National Centers for Environmental Prediction (NCEP) Climate Forecast System version 2 (hereafter referred to CFSv2) strategy at the Indian Institute of Tropical Meteorology (IITM), Pune and monsoon modelling communities under the Ministry of Earth Sciences (MoES) to deliver dynamical operational forecast since 2011, there has been a growing need for rigorous evaluation of the skill of NCEP-CFS model in terms of the capability of simulating the MISOs as well as the total rainfall amount in the extended range. Since MISOs explain the dominant variance in the intraseasonal scale[14,15], the skill of quantitative precipitation forecast is naturally tied to the prediction skill of MISOs. The ERP skill of tropical ISOs as well as MISOs of any dynamical model depends on several factors[16,17], and various studies have exhibited the unambiguous role of the coupled evolution of the ocean–atmospheric mode in the coupled general circulation models (CGCMs). A faithful representation of the air–sea interaction in these coupled models is a dominant factor to generate the 'observed' mode of the intraseasonal propagation[18–20].

Before the development of the state-of-the-art CGCM in which the sea surface temperature (SST) is evolved synchronously with the atmospheric components, the atmospheric general circulation models (AGCMs) have been used for the diagnostic analysis and forecast of MISOs. These studies used the SST as lower boundary forcing to simulate the MISOs and discussed the impact of SST lower boundary forcing on the prediction of MISOs[21–24]. All these studies advocate the fact that the simulation and prediction of MISOs using dynamical models is delicately dependent on the climatological mean condition of the model-simulated large-scale dynamical environment (e.g. zonal and vertical winds, etc.). In this sense, it is debated whether the MISO is largely an atmospheric component and/or the interacting SST in the coupled models has such a significant role in predicting the structure and propagation of MISOs. Recently, Rajendran *et al.*[25] claim that the role of SST coupling is passive, and AGCMs with realistic SST boundary forcing can simulate the SST–rainfall relationship on the interannual scale reasonably well, and thus may give a reasonable dynamical prediction of the interannual variability[26]. This conclusion may not naturally be extended to intraseasonal scale. A series of studies in the last decade however showed that the surface heat fluxes and ocean dynamics might have substantial impact in the simulation, prediction skill and also the predictability of

*For correspondence. (e-mail: sahai@tropmet.res.in)

the tropical ISOs in general[18,27–40]. It has also been shown that the role of intraseasonal SST–rainfall lag–lead relationship over the Bay of Bengal (BoB) and Arabian Sea (AS) is critical for the northward phase propagation of MISO during active and break spells[41–43], and thus may be important in predicting the active/break spells over Central India (CI). In addition, a number of modelling studies have also demonstrated that the CGCM not only simulates a stronger ISO than the AGCM, but also generates a realistic phase relationship between intraseasonal convection and underlying SST[39,44–51]. However some studies, especially on Madden–Julian oscillation (MJO) and equatorial waves, also indicate that inclusion of air–sea coupled processes may not always lead to improvements for the same[38,52–55]. On the contrary, Seo *et al.*[46] concluded that '*Improvements tend to occur when coupled models are capable of simulating observed relationships among convection, surface heat fluxes, and SST associated with the ISO, and in such cases the ISO in the coupled model simulations are indeed improved compared with the simulations in the atmosphere-only integrations.*'

Thus, although it is well established that the representation of MISOs in CGCM is more reasonable than AGCM, it is not yet apparent to what extent, in general, the realistic representation of air–sea interaction in CGCM influences the real-time prediction of the northward phase propagation of MISOs in the extended range. It is also not obvious to what extent the biases in simulated SST in CGCM impact the MISO phase propagation and statistical relationship of SST with rainfall over Indian monsoon region. In addition, if such daily SST biases in CGCM are further corrected with respect to observed daily SST and then reassigned as the corrected boundary forcing for AGCM, will it be realistic enough to simulate and predict MISOs in the extended range? Focusing on these questions based on SST–rainfall relationship, is essential to develop a realistic operational forecast system for ERP of MISOs based on the recent version of NCEP-CFS/GFS models. Seo *et al.*[46] have used the previous version of NCEP-CFS model and demonstrated the role of SST and the air–sea coupling for the propagation of the boreal summer ISO. In this study, we take these issues further and focus on the role of the air–sea interaction in NCEP-CFS/GFS model adopted in IITM for the prediction of MISOs. Precisely, we attempt to address the following scientific issues in this article:

(i) What is the skill of CFS and GFS models in capturing the northward phase propagation and rainfall–SST relationship?
(ii) What is the performance of GFS and CFS in the real-time prediction of MISOs for the ISM season of 2011 and 2012?

To answer the above questions, we need to simulate the ISM and its variability in AGCM and CGCM under identical settings. In this study, both AGCM and CGCM share the same atmospheric model, which ensures the identical dynamical core and parameterization of the atmospheric component. We have made long free runs using both AGCM and CGCM to evaluate the inherent model biases that may influence the rainfall–SST statistics. Details of the models, experiment design and observed dataset used are discussed in the following sections respectively. Next, we discuss results from the long runs and the hindcast experiments. This is followed by summary and conclusions.

Model description

The CGCM used in this study is the NCEP-CFS coupled model version 2 (refs 56 and 57). The atmospheric component of the model is NCEP-GFS at T126 resolution (approximately 100 km) with 64 vertical levels, which is coupled to the NOAA Geophysical Fluid Dynamics Laboratory (GFDL) modular ocean model version 4 MOM4 (ref. 58), sea-ice model and Noah land model. The ocean model is a finite difference version of the ocean primitive equations configured under the Boussinesq and hydrostatic approximations with zonal resolution of 1/2° and meridional resolution of 1/4° between 10°S and 10°N, gradually increasing through the tropics to 1/2° poleward of 30°S and 30°N. There are 40 layers in the vertical with 27 layers in the upper 400 m of the ocean, and the maximum depth is approximately 4.5 km. The vertical resolution is 10 m from the surface to 240 m depth, gradually increasing to about 511 m in the bottom layer.

Data and methodology

Two different sets of experiment have been conducted to evaluate the mean biases ascribed to both AGCM and CGCM in simulating the chief features of MISOs and further to assess the prediction skill and performance of both AGCM and CGCM in real-time ERP of rainfall associated with the active–break spells of ISM. In the first set of experiments: two types of free long runs are performed: (i) CFS coupled run for 100 years and (ii) GFS run forced with bias-corrected CFS simulated daily SST for 30 years. Figure 1 shows the seasonal mean (June–September, JJAS) SST bias produced by CFS. It shows that CFS suffers a systematic cold bias that dominates globally, except some parts in the west coast of Mexico and Ecuador. These biases are as large as 2–4°C in some regions and most importantly, it has larger amplitude over the Indian Ocean (IO) compared to the equatorial Pacific. We identified the daily SST bias in CFS and corrected it with respect to the observed daily SST data (OISST). Bias correction is done by removing the daily mean bias (model daily climatology – observed daily

climatology) from the daily forecasted SST. This corrected daily SST is provided as the boundary forcing for the 30-year-long simulation using GFS. Finally we analyse the last 55 years of CFS simulation and 25 years of GFS simulation for the present study.

Next, for the real-time forecast experiments, both GFS and CFS were integrated for 25 days in ensemble mode. Here, both GFS and CFS models share the same sets of 11 atmospheric initial conditions and the AGCM GFS is forced with bias-corrected SST forecasted from corresponding unperturbed CFS forecast. Each ensemble member is generated by slightly perturbing the initial atmospheric conditions (the control run initial conditions have been prepared from coupled data assimilation system (CDAS) with T574L64 GFS-based atmospheric assimilation and MOM4-based oceanic assimilation). In order to make the perturbation size consistent with analysis variance of each variable in the perturbed initial conditions, the amplitudes of perturbation are adjusted to ensure sufficient spread in the forecast fields[59]. For the CFS/GFS output validation, the following available observational and reanalysis datasets have been used: (a) monthly and daily precipitation data from Global Precipitation Climatology Project (GPCP[60,61]), (b) daily gridded rainfall data from National Climate Centre, India Meteorological Department[62], (c) the TRMM-gauge merged rainfall dataset[63] from India Meteorological Department (IMD), (d) daily data of circulation at different vertical levels from NCEP–NCAR Reanalysis data[64] and (e) daily NOAA OISST (http://www.esrl.noaa.gov/psd/). The observation field is hereafter referred to as OBS in the following discussion.

Results

Long-run comparison: the climatological and statistical aspects

The realistic simulation of the climatological seasonal mean (JJAS) precipitation as well as the atmospheric large-scale circulation is an essential factor for reasonable representation of the ISM variability. We compare the JJAS mean precipitation (shaded) and low-level (850 hPa) wind (vector) simulated in long runs of CFS (Figure 2 *b*) and GFS (Figure 2 *c*) with the observed precipitation and wind (GPCP and NCEP-NCAR; Figure 2 *a*). The large-scale seasonal biases in the respective models are further depicted in Figure 2 *d*, *e*. We highlight some of the important points apparent from Figure 2 as follows:

- CFS shows considerable dry bias in precipitation over Indian land region, while GFS could capture the observed pattern of rainfall reasonably well. However, the oceanic convergence zone over equatorial IO and equatorial western Pacific region is poorly simulated in GFS run compared to CFS. The pattern correlation for the larger South Asian region (40°–140°E; 15°S–35°N) between GPCP and GFS (CFS) is 0.66(0.8). It is also to be noted that the amount of rainfall over the oceanic convergence zone of equatorial IO and equatorial western Pacific region is too strong in CFS and too weak in GFS.
- The low-level cross-equatorial flow and the cyclonic circulation over the ISM region are well reproduced by CFS. However, GFS shows an erroneous strong westward low-level flow near the equator, with the separation between the continental and oceanic convections. Over the extended monsoon region, both GFS and CFS over-estimate the wind vectors compared to OBS.
- The overall large-scale structure of the northern convergence zone, the hallmark of climatological monsoon circulation, is confined to the Indian region only and does not extend to the Maritime continent in GFS, whereas it is well captured in the CFS.
- GFS has considerable dry bias over the equatorial IO and equatorial western Pacific compared to observation.

Thus we can deduce that GFS alone, even though it simulates better rainfall climatology over Indian land mass in the sense that the dry bias is reduced to some extent over the areas adjoining the east coast and BoB, does not represent the true large-scale climatology of GPCP pattern. The impact of bias correction in SST forcing thus does not have much influence in correcting the mean state of the model atmosphere in general.

We further examined the local SST–rainfall lead–lag relationship for daily data over the IO region which is characterized by a large range of variation of SST and also has large impact on the Indian monsoon and its interannual variability, as similarly shown in monthly scale by Rajendran *et al.*[25]. The fidelity of coupled model-simulated daily SST relationship can be seen in the local SST–rainfall lag–lead relationship plot in Figure 3). The area-averaged SST over grid points as mentioned in the panels is used as a reference time series and the correlation

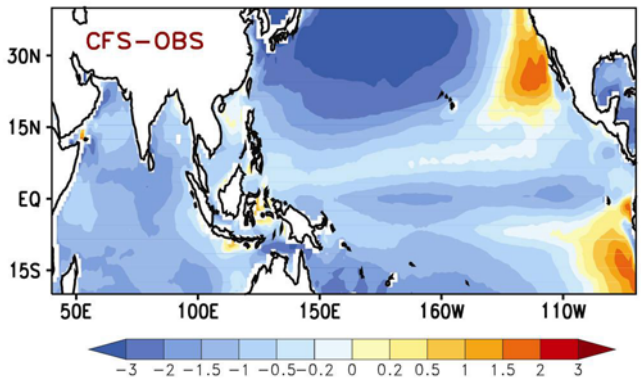

Figure 1. Seasonal (JJAS) bias of CFS-simulated SST from OISST.

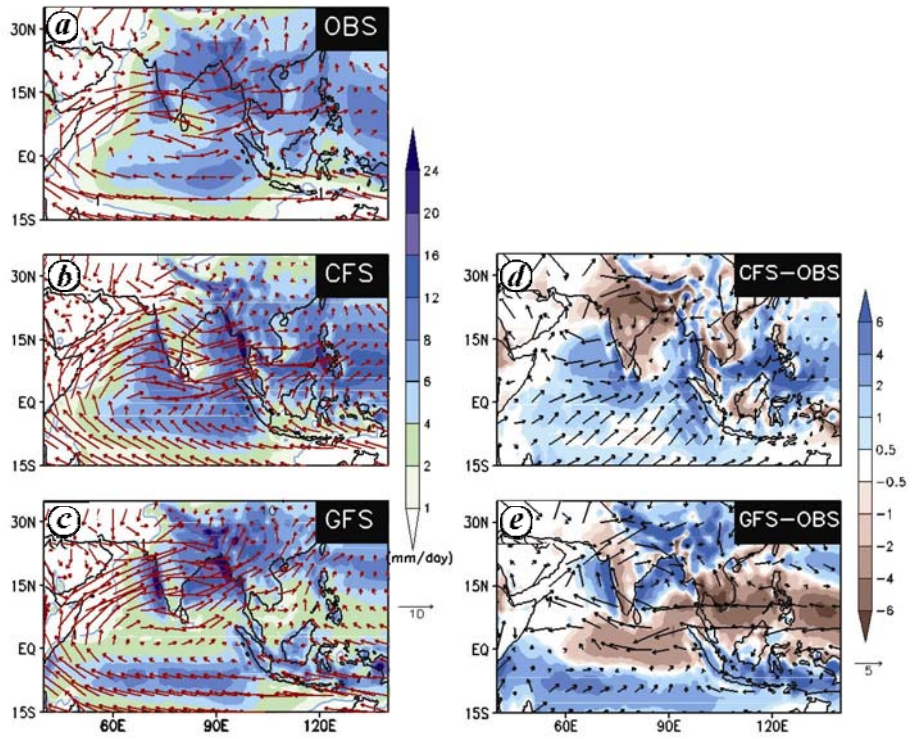

Figure 2. Seasonal (JJAS) mean precipitation (mm/day, shaded) and low-level (850 hPa) circulation (m/s, vector) for (***a***) OBS (GPCP), (***b***) CFS and (***c***) GFS. JJAS precipitation bias in (***d***) CFS and (***e***) GFS (bias-corrected SST).

of SST with rainfall is plotted as a function of lag–lead time. Figure 3 *a* shows the correlation over AS and Figure 3 *b* shows the same over BoB. It is evident from the figure that over both the regions CFS outperforms GFS. However, it may also be seen that the lag-correlation relationship is different over the two regions in OBS simulation. Over BoB, the lag correlation peaks at –10 days (other than lag 0), while over AS the lag correlation in OBS peaks around ~5 days. Nevertheless, the AS has better lag–lead relationship in CFS than BoB. Over BoB, there is a shift in peak of about 1–2 days (blue and black curve), while over the AS both peaks are at the same lag. Recently, Roxy *et al.*[65] have observed similar behaviour and attributed this to the realistic simulation of oceanic processes. The fall of correlation in GFS at higher lag implies that the low-frequency component cannot be predicted more than on weather range, typically pointing a Markovian nature (red-noise) of the temporal evolution. However, increase in correlation at higher lag for CFS simulation can be taken as an indicator of higher chance of a long-range periodic forcing with higher predictability in the extended range beyond weather scale, consistent with the theory of MISO prediction (similar to predictor–predictands relationship in a good statistical model). Another evidence of improvement is given in Figure 4, in which we show the composite northward propagation of MISO from the GPCP, CFS and GFS long run. The northward propagation is plotted using a lag-regression technique with CI area-averaged rainfall as a reference time-series. Here, it is apparent that the rainfall phase propagation in CFS initiates from the oceanic region as in observations, while such phase propagation is not clear in GFS. However, interestingly the negative anomalies of convection show some propagation in GFS. This shows that the air–sea interaction during convectively active phase is more actively participating in the realistic phase propagation. The above analysis reveals that though the MISO is typically an atmospheric component, many of its features and lag–lead relationship of the large-scale boundary forcing (e.g. SST) with the predictand (rainfall) are well captured by a coupled model (CFSv2) than the atmospheric stand-alone model (GFS). Thus the coupled model is expected to improve the simulation and prediction of MISOs.

The statistical aspects of this deficiency in capturing the SST–rainfall relationship would be revealed from a co-spectrum plot indicating the co-variability of the same two variables. This is shown in Figure 5 for the data averaged over AS region**.** The top row shows the co-spectrum, coherence and phase relationship of the two variables, rainfall and SST from OBS. The middle and bottom rows show the same from GFS and CFS runs respectively. It is clear from the co-spectrum and coherence plot that in the intraseasonal range (abscissa between frequency 10^{-1} and 10^{-2} day^{-1}) the co-variability is comparable between OBS and CFS, but GFS shows

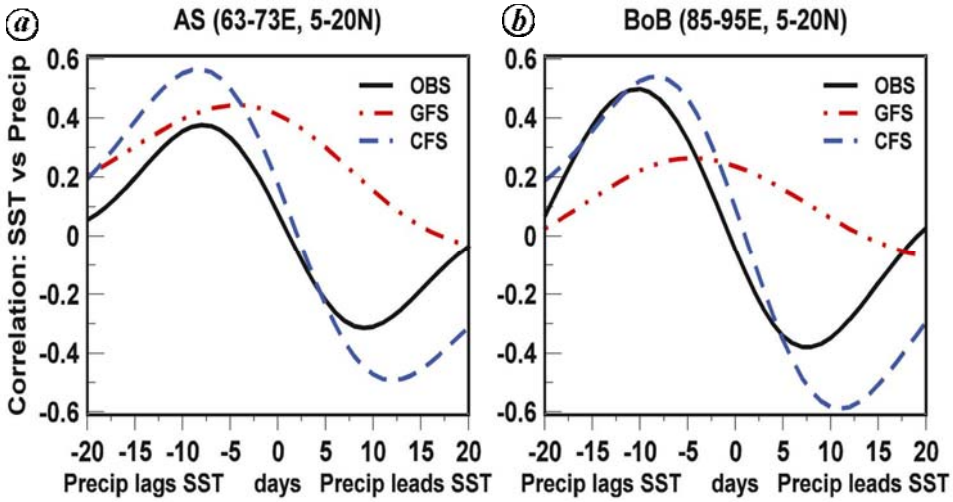

Figure 3. Lag–lead correlation of daily precipitation anomalies with respect to daily SST anomalies on intraseasonal timescales (20–100 day filtered) averaged over (***a***) AS (63–73°E; 5–20°N) and (***b***) BoB (85–95°E; 5–20°N) for OBS (black curve), CFS (blue curve) and GFS (bias-corrected SST, red curve).

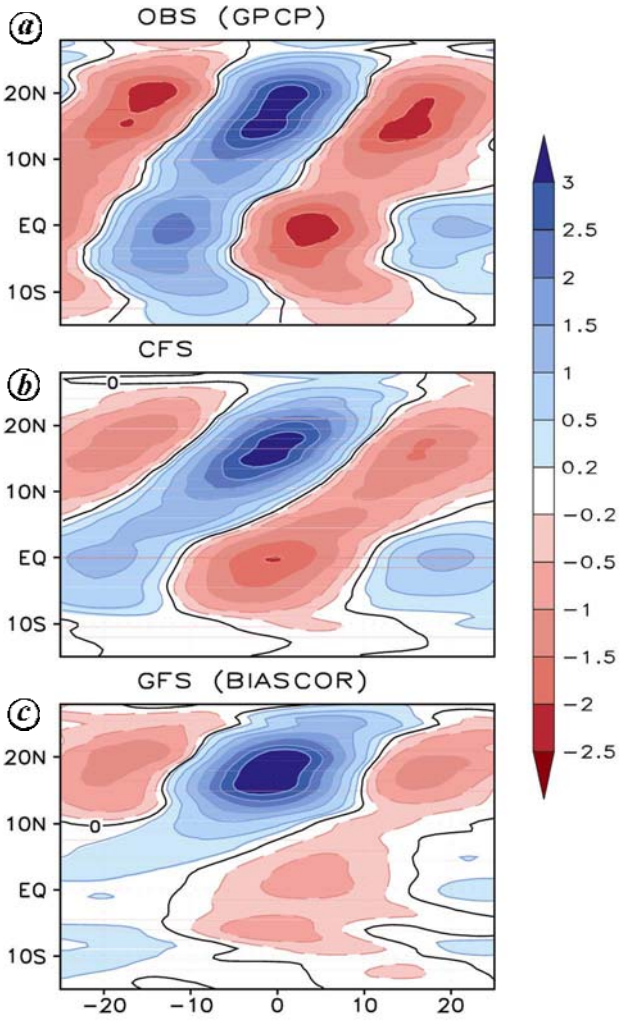

Figure 4. Time–latitude plots of regressed precipitation anomalies (20–100 day filtered; mm/day) averaged over 65–90°E for observation and model runs: (***a***) OBS, (***b***) CFS and (***c***) GFS (bias-corrected SST).

unrealistic variability compared to OBS. A prominent deficiency is also seen in the phase plot for all the variables. The phase difference between rainfall and SST of about 100° is clear in OBS as well as in CFS in the intraseasonal low frequency range. However, GFS does not show any such phase shift. This phase is the arc-tangent of the co-spectrum and the quadrature spectrum. For two completely random variables, it will fluctuate randomly as is clear in any of the panels beyond frequency of 10^{-1} day^{-1}. This implies that below a periodicity of 10 days, there is no phase relationship between SST and rainfall and they are statistically independent. However, in the lower frequency (i.e. intraseasonal) range, the OBS data show a fixed phase relationship. The wild fluctuation of phase angle is intruded in the intraseasonal range in the GFS plot, whereas CFS fluctuation matches with the OBS. Thus, the CFS run is able to capture the statistical phase dependence closer to OBS between the variables SST and rainfall. This relationship between rainfall and SST is similar in the BoB region also (figure not shown).

Comparison of 2011 and 2012 forecasts using CFS and GFS

Operational real-time prediction: The panels of Figure 6 shows the observed JJAS evolution of precipitation for 2011 and 2012. Figure 6 *a* and *b* shows the pentad evolution of rainfall anomaly (%), while Figure 6 *c* and *d* shows the 20–80 day filtered Hovmöller diagrams of daily precipitation anomalies averaged over 60–95°E. From Figure 6 *a* and *b*, it is noted that there are few active spells identified for both 2011 and 2012 towards the end of season (the transition to active happened in the last week of August and first week of September). These active spells are also associated with northward-propagating

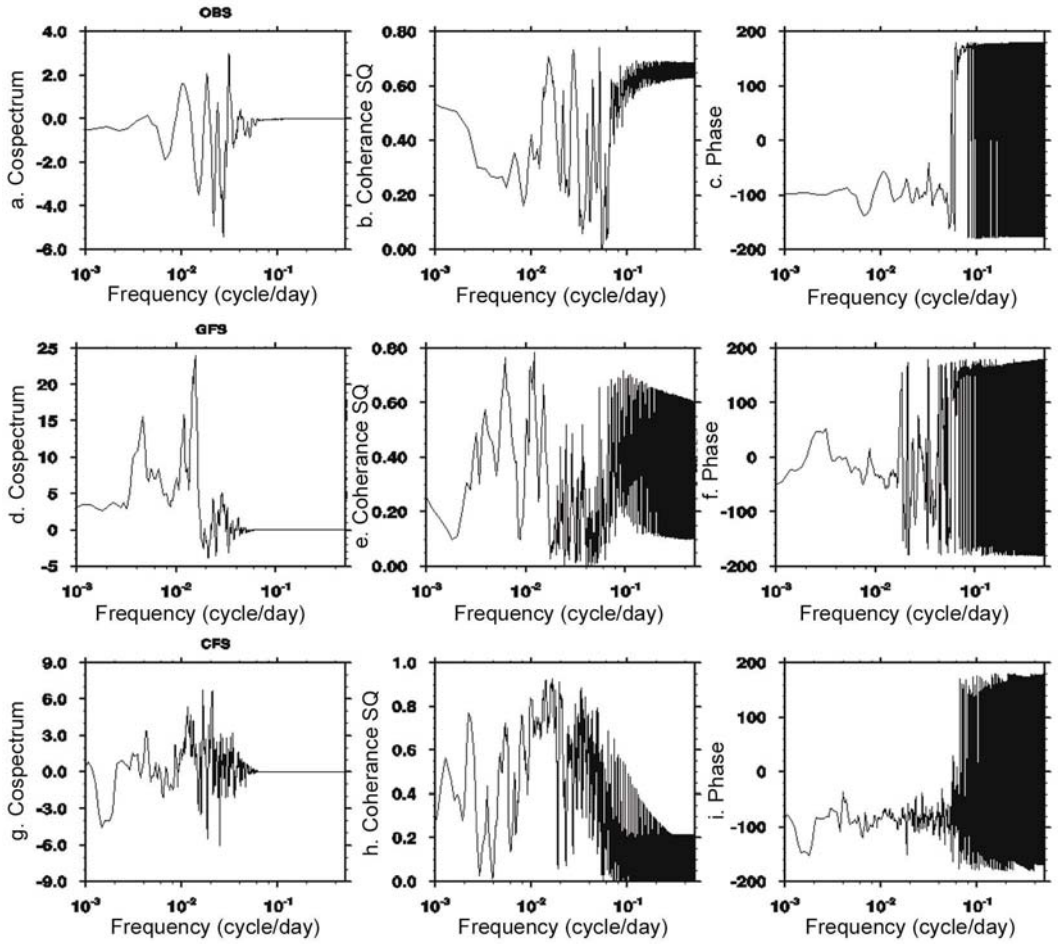

Figure 5. The co-spectrum (left column), coherence (middle column) and phase relationship (right column) between daily rainfall and daily SST: OBS (top row); GFS (bias-corrected SST, middle row); CFS (bottom row).

Table 1. Correlation coefficients for the monsoon zone rainfall for 24 pentads during 2011 and 2012. CC values are shown up to four pentad lead for GFS and CFS

	2011		2012	
	CFS	GFS	CFS	GFS
P1-lead	0.64	0.63	0.74	0.90
P2-lead	0.33	0.60	0.34	0.76
P3-lead	0.12	0.41	0.53	0.30
P4-lead	0.43	0.35	0.38	–0.22

positive rainfall anomalies, as seen in Figure 6 *c* and *d*. We mark arrows on two selected pentads in this plot which are the transition to active spell that will be discussed in detail later. In order to observe the deterministic (ensemble mean) skill of rainfall prediction using CFS and GFS for these two years, Table 1 provides a relative comparison of forecast skill in different pentads. It may be seen that for pentad 1 and pentad 2, the forecast skill of GFS forced with bias-corrected SST is at par or higher than CFS-coupled SST. The GFS forecast skill linearly decreases with time, while CFS forecast skill is improved at later lag. This may be an artifact of the SST–rainfall relationship as seen in Figure 3. The SST–rainfall relationship shifts to strong anti-correlation at later lags. This strengthening of (opposite) relationship at later lead time may be due to the periodic forcing imposed by northward propagating MISOs. It is evident that CFS simulates the MISOs more realistically, with better phase relationship between convection over Indian land region and equatorial IO, compared to GFS. Therefore, the error growth in the actual forecast in CFS may be less if the forecast starts with an initial time when the convection is over IO. Thus the reduction in forecast skill with increase in lead time due to stochastic error growth seems to be partly compensated by better phase representation of phase relationship of convection in CFS over the Indian region due to improved air–sea interaction compared to GFS, that leads to slight improvement in correlation skill at the fourth pentad in both years in CFS.

Figures 7 and 8 show the prediction verification for four selected pentads based on the active spells identified in Figure 6 (marked as arrows). The prediction of the

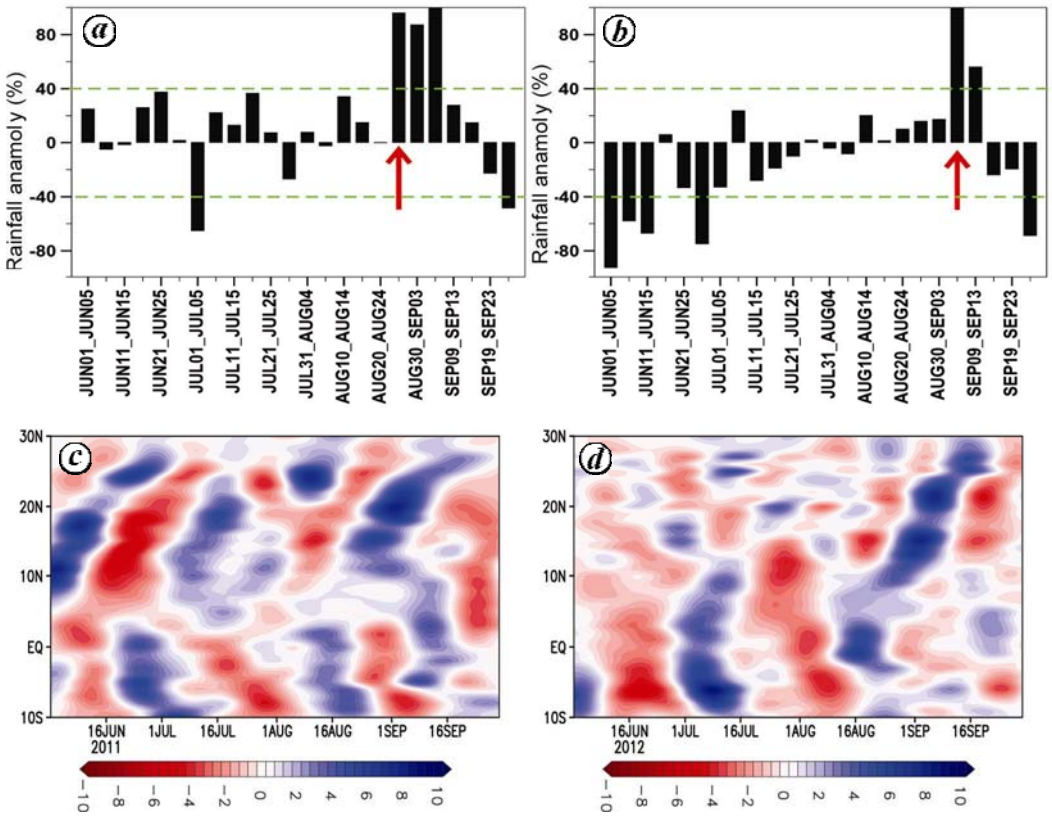

Figure 6. JJAS pentad mean percentage anomalies over monsoon zone: (***a***) 2011, (***b***) 2012 and 20–90 day filtered anomalies averaged over 60–95°E from 1 June to 30 September, (***c***) 2011 and (***d***) 2012.

active pentads for the years 2011 (25–29 August) and 2012 (4–8 September) are shown in these figures respectively. These pentads represent a transition to the strong active conditions and they are plotted to demonstrate the fidelity of the models in capturing this transition. The 2011 case represents a strong active condition over the west coast and northwest India (Figure 7, top panel). Figure 7 shows that the CFS model is able to capture the transition to active spells over these regions four pentads in advance, while GFS shows mostly negative to no rainfall anomaly over this region when forecast 3–4 pentads in advance. For 2012, the 4–8 September spell has active conditions prevailing over south-central India and adjoining BoB (Figure 8 top panel). This spell is captured with improved fidelity four pentads in advance in the CFS model compared to GFS. Thus, the transitions to active spells are predicted well in advance in CFS with better skill in terms of spatial patterns of observed distribution of rainfall.

Ensemble mean and probabilistic forecast of 2011 and 2012 over monsoon zone: The ensemble mean and probabilistic forecast for area-averaged rainfall over monsoon zone for the years 2011 and 2012 in the third and fourth pentad lead time are shown in Figures 9 and 10 respectively. The top panels show the third pentad forecast and the bottom panels show the fourth pentad forecast. The left panels show the plots for CFS forecast whereas the right panels show the plots for GFS forecast. Each panel consists of four sets of sub-panels. The top subpanel shows the pentad mean percentage rainfall anomalies for the observed (brown bars) and ensemble mean prediction (green bars). The two horizontal lines (blue) show the ± 40% pentad departure anomaly line. The rainfall above (below) 40% (–40%) anomaly is categorized as active (break) spells or else as normal spells when it remains within ± 40% range. The probabilistic forecast, i.e. the percentage of ensemble member in active (navy blue), normal (sky blue) or break (orange bars) category is shown in the bottom three subpanels of each panel respectively. For the year 2011 as shown in Figure 9, the strong active spells during the end of August–mid September are captured in CFS when predicted third and fourth pentad in advance. Although the GFS shows fidelity in capturing the active–break spells in the third pentad, it cannot forecast the active spell in a four-pentad lead time. Similarly, the strong active spell in 2012 (Figure 10) during the end of season, is also better forecasted in CFS compared to GFS. Moreover, the break spell in the first two weeks of June is also coherently captured in CFS. The GFS, however, does not skillfully predict the break spell four-pentad in advance.

The quantitative verification of CFS and GFS probabilistic forecast skill for the entire 2011 and 2012 season (48 pentads) could be shown using a relative operating characteristic (ROC) curve[66]. This is basically a graph between hit rate (HR) and false alarm rate (FAR) for each category forecast (i.e. active, break and normal category). HR is defined as the proportion of occurrences, when both the observed rainfall and the forecasted rainfall are in the same category. Similarly, FAR is defined as the proportion of non-occurrences, i.e. when forecasted rainfall is not in the observed category. For all the pentads in 2011 and 2012 from June to September HR and FAR may be obtained and binned as frequency of occurrence. The scatter plots of the binned HR and FAR are shown in Figure 11. The triangular portion below the dotted diagonal line shows the region where FAR ≥ HR, and hence may be considered as region of no skill forecast. Any forecast (represented by lines for each category), above this line is case when HR ≥ FAR and hence may be considered as useful forecast. A useful measure of quantitative forecast skill is area under the curve (AUC) defined as the net area enclosed by the curves (Figure 12). It may be easily seen from Figures 11 and 12 that the forecast skill of CFS is much better in the fourth pentad lead time compared to GFS. For all other pentads, both CFS and GFS show comparable skills. Figure 11 shows that break and normal categories are poorly forecasted in GFS pentad-4 in advance compared to CFS forecast. In pentad-2 lead time, Figures 11 and 12 show that active spells are better predicted in GFS compared to CFS. Thus the probabilistic skill score shows improvement in CFS forecast skill compared to GFS forecast with bias-corrected SST with a lead time above 10 days.

MISO forecasts of 2011 and 2012: The MISO forecasts in extended range are important for agricultural and hydrological purposes. We check the forecast skill of CFS and GFS for the years 2011 and 2012. Recently, Suhas *et al.*[15] have developed an index for real-time monitoring and real-time validation of MISO forecast similar to the Wheeler and Hendon index of MJO[67]. The paper defines two indices MISO1 and MISO2, which are

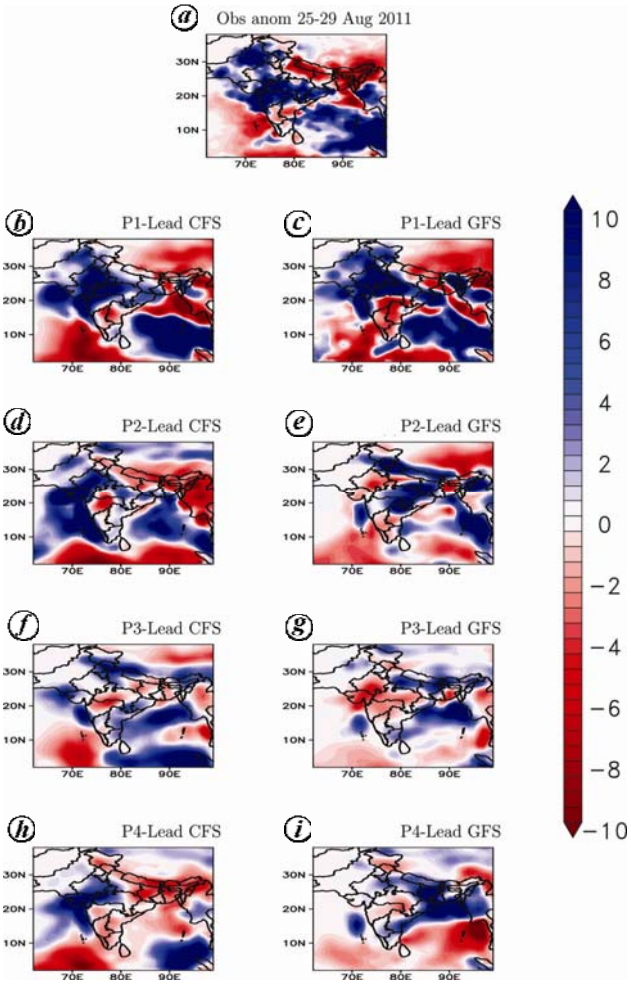

Figure 7. Transition to an active phase during 25–29 August 2011. Rainfall anomalies are plotted for (***a***) observed, forecast valid for lead pentad 1, (***b***) CFS, (***c***) GFS, lead pentad 2, (***d***) CFS, (***e***) GFS; lead pentad 3, (***f***) CFS, (***g***) GFS; lead pentad 4, (***h***) CFS and (***i***) GFS.

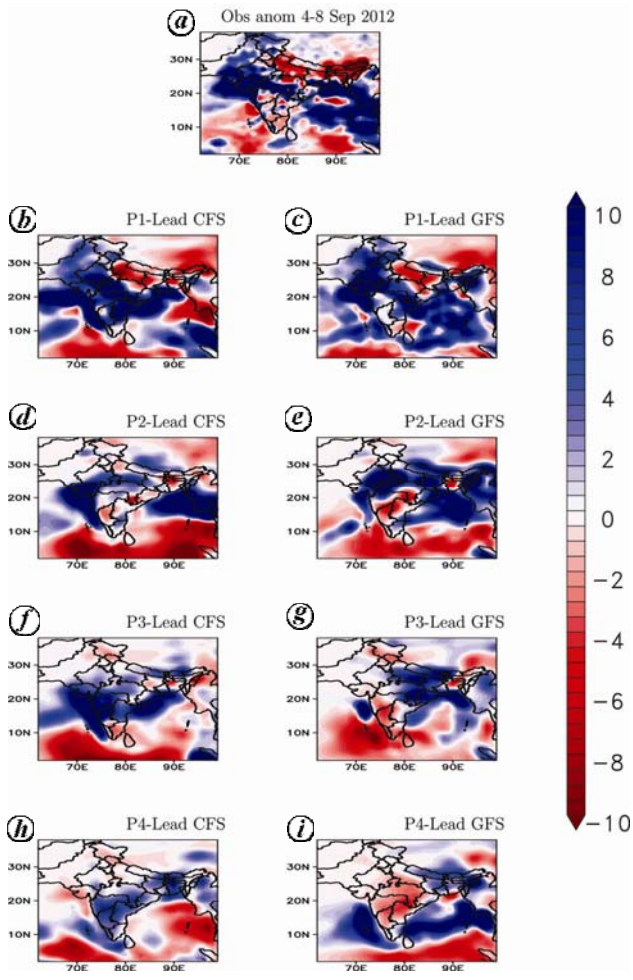

Figure 8. Transition to an active phase during 4–8 September 2012. Rainfall anomalies are plotted for (***a***) Observed, forecast valid for lead pentad 1, (***b***) CFS, (***c***) GFS; lead pentad 2, (***d***) CFS, (***e***) GFS; lead pentad 3, (***f***) CFS, (***g***) GFS; lead pentad 4, (***h***) CFS and (***i***) GFS.

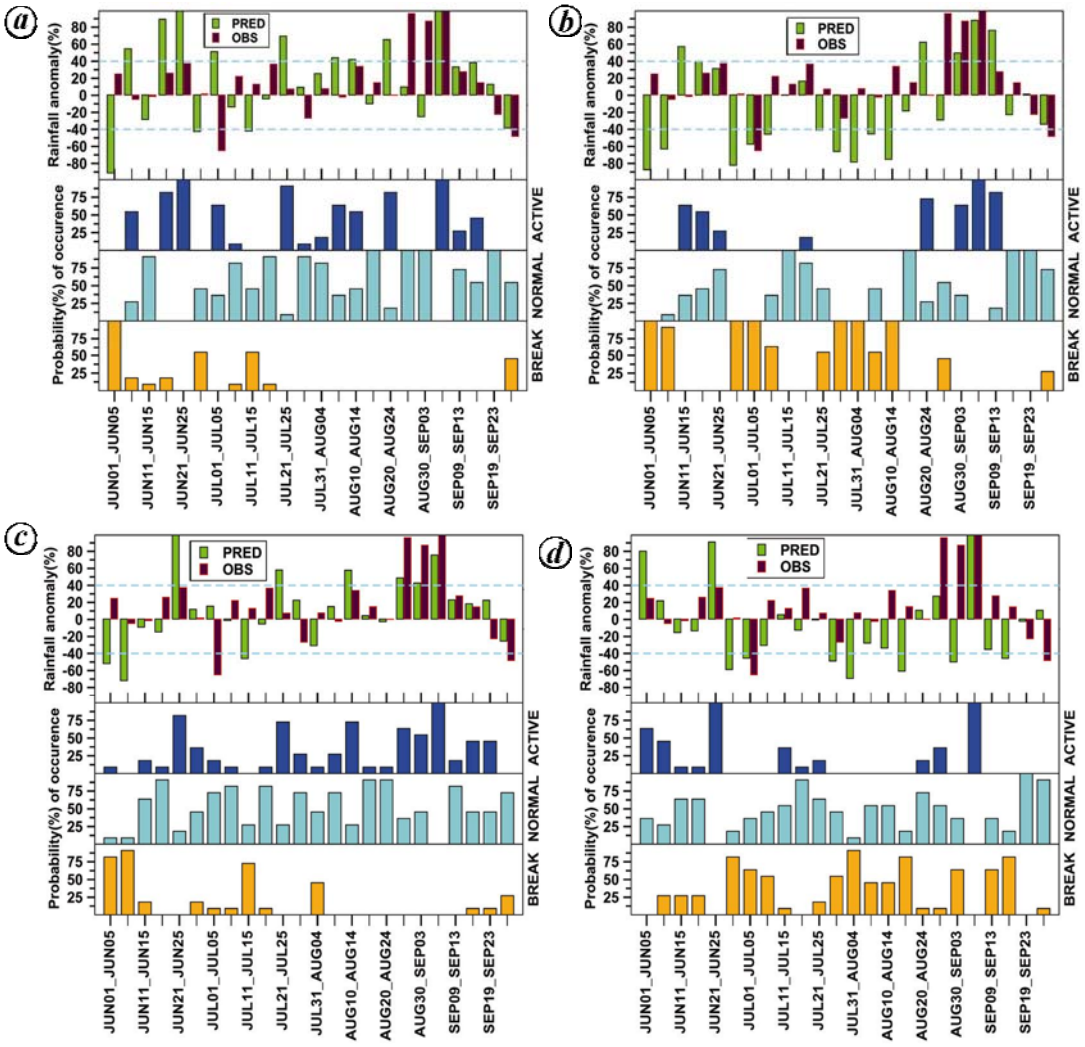

Figure 9. Observed and forecasted rain anomalies and forecast probabilities for three categories (active, normal and break) over monsoon zone during 2011. Pentad 3 and pentad 4 are shown for CFS in (***a***), (***c***) and those for GFS (bias-corrected SST) in (***b***), (***d***).

the principal components of extended empirical orthogonal functions (EEOFs). The EEOFs are obtained based on a covariance matrix created from 60°E to 95°E averaged rainfall data extending from 15°S to 35°N for the 122 days of monsoon season of 12 continuous years (1998–2009). The EEOFs show latitudinal variation in the data and the favourable region of convection. These principal components (MISO1 and MISO2 indices) explain about ~ 23% variances in the data. The index captures the large-scale low-frequency northward propagation of MISO. Since the amplitude of MISO1 and MISO2 for any day represents the northward-propagating components, the scatter plot of MISO1 versus MISO2 time series would show the evolution of MISO. The scatter plot can be divided into eight equal octants and a composite of any day residing in each octant would represent a location of convective anomaly. A systematic propagation of convective anomalies will be obtained based on the composite of precipitation for the days clustered in each octant (also called phases) of the scatter plot (see figure 8 of Suhas *et al.*[15]). For more details, refer to Suhas *et al.*[15]. The northward propagation and real-time monitoring of MISO for the years 2011 and 2012 are shown in Figure 13 *a* and *b* respectively. Here each octant or phase is represented as a pizza slice. The phase index (1–8) and the location of convection band in the respective phases are mentioned at the top of each pizza slice (black dotted line). The dotted unit circle ($MISO1^2 + MISO2^2 = 1$) is also shown. Amplitude of MISO indices below the unit circle may be considered as insignificant. The plot for 2011 (Figure 13 *a*) shows that the MISO amplitudes are weak over CI most of the time, while northern India and foothills of the Himalaya show strong MISO amplitude during September. Also June and July show strong MISO amplitude over the southern peninsula and IO, but the amplitudes are not propagated to CI and the monsoon zone. For 2012, it also shows strong MISO amplitude started from end of August over CI or monsoon zone (Figure 13 *b*).

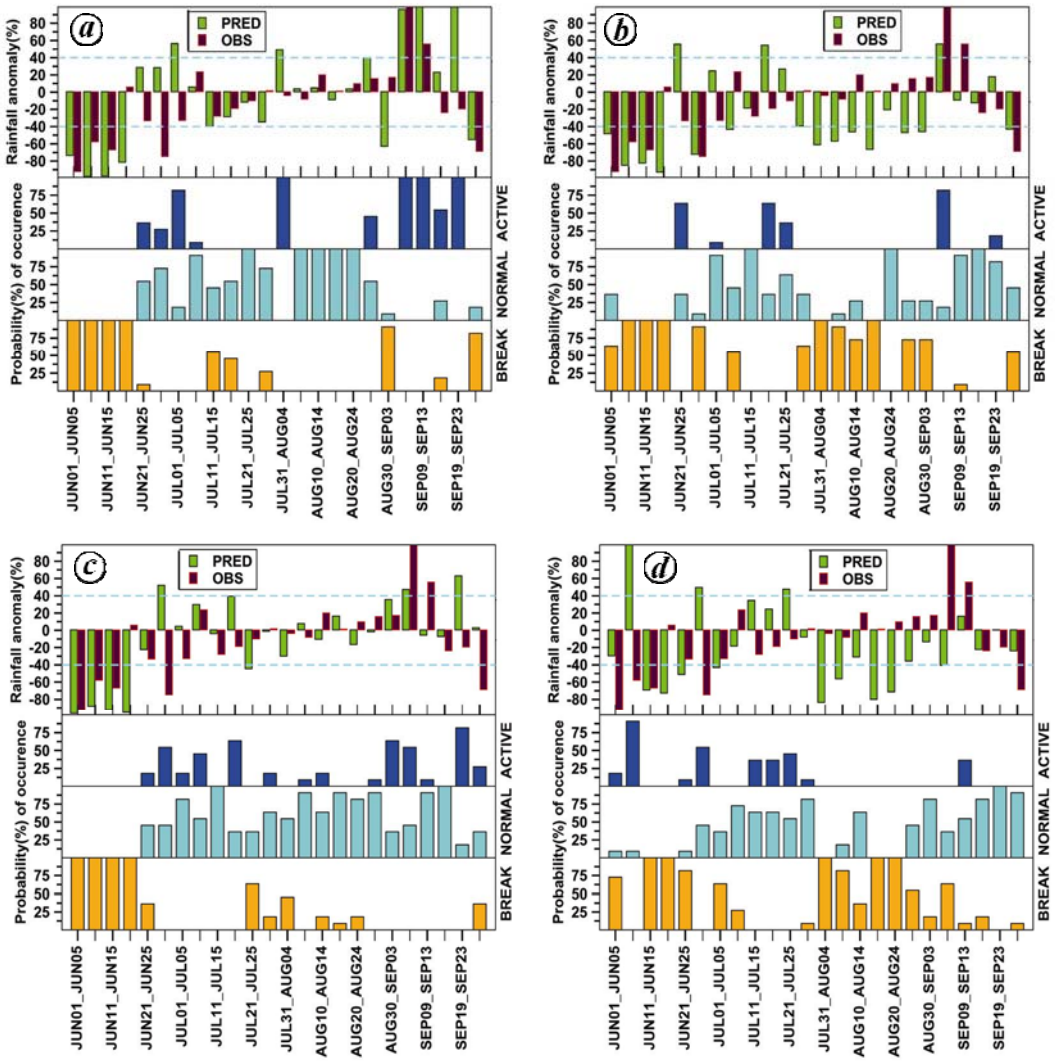

Figure 10. Observed and forecasted rain anomalies and forecast probabilities for three categories (active, normal and break) over monsoon zone during 2012. Pentad 3 and pentad 4 are shown for CFS in (***a***), (***c***) and those for GFS (bias-corrected SST) in (***b***), (***d***).

Figure 14 *a*, *b* shows the forecast skill (correlation) of MISO indices and MISO amplitude $(MISO1^2 + MISO2^2)^{0.5}$ as a function of lead time using CFS and GFS for 2011. The skills are shown for 18 cases of real-time forecasts during June–September of 2011. The MISO amplitude (green curve) shows 15-day lead skill, whereas for GFS it is 13 days before the correlation becomes insignificant (< 0.6). Also, MISO1 shows better skill in CFS compared to GFS. However, the forecast skill of MISO2 is relatively better in GFS compared to CFS. Since the MISO amplitudes represent the net variances explained by the MISO using EEOF method, the overall improvement in skill is obtained from MISO amplitude, which is two days more in CFS compared to GFS. Figure 14 *c–f* shows the phase evolution of MISO starting from four initial conditions (mentioned at the top of each panel) to capture an active condition starting around pentad 25–29 August 2011 over North and Central India. The blue curve shows the observed phase evolution for next 20 days starting from an initial condition in each panel. The red curves show GFS ensemble members, whereas green curves show CFS ensemble members. It may be seen that both CFS and GFS show identical behaviour in capturing the phase evolution, although the amplitude differs at times with observation. The initial condition from 24 August (Figure 14 *f*) shows large over-estimation of MISO amplitude using CFS compared to GFS. Figure 15 shows the same plot as Figure 14, but for 2012 and for active pentad starting during 3–7 September 2012. Figure 15 *a* and *b* shows identical skill in MISO index amplitude forecast (~ 10 days) for both CFS and GFS. However, individual indices (MISO1 and MISO2) are better predicted in GFS run with bias-corrected SST in this year. Finally, Figure 15 *c–f* shows that although the phase

propagation is captured from different initial conditions here, the amplitudes are overestimated compared to observations. CFS-derived MISO amplitudes show larger over-estimation than GFS in general 5–7 days after the start date of forecast.

Discussions and conclusions

The realistic SST–rainfall on subseasonal range relationship has long been considered as an important indicator of the fidelity of models in simulating as well as predicting the MISOs during the summer monsoon season. In this study, we experimented with NCEP-CFS coupled model (CFSv2) and the atmospheric component of the same (i.e. GFS) forced with bias-corrected daily SST to study the role of SST in capturing the climatological features and the intraseasonal SST–rainfall relationship in general with an aim to understand the importance and role of this relationship in the simulation of northward phase propagation and the prediction of MISOs. It is shown that the local SST–rainfall lag–lead relationship (Figure 3) is more realistic in the CFS model. Inability of GFS in capturing this feature would have important consequences in the large-scale dynamical feedback. Inappropriate representation of phase change in periodic forcing as evident from cross-correlation curve in GFS compared to CFS with respect to observation would lead to unrealistic rainfall amplitude in GFS associated with MISO. Since the large-scale rainfall is always associated with MISO, such errors in rainfall may impart large errors on the circulation. Also, this SST–rainfall relationship is important in capturing the phase propagation of the MISOs, also shown by Roxy *et al.*[65] using a similar modelling strategy with CFS. The gradual fall (rate of change) of cross-correlation curve for GFS compared to OBS and CFS runs may indicate the temporal longer-range persistence or long-range memory in GFS (for dependence of cross/auto-correlation on long-range memory of time-series refer to Carreras *et al.*[67], Zhou[68], Zhu *et al.*[69]). In CFS run similar to OBS, the de-correlation lead-time below significance level is reached much earlier than GFS. Thus cross-correlation function may be influenced by artificial and model-induced long memory in GFS. This may be an artifact of the absence of proper air–sea interaction, which is efficiently captured in the coupled CFS run. Hence, the northward phase propagation in CFS is efficiently captured. In spite of this, the dry bias in rainfall over the Indian land mass is present dominantly in the CFS and although reduced to some extent, it is present in the GFS.

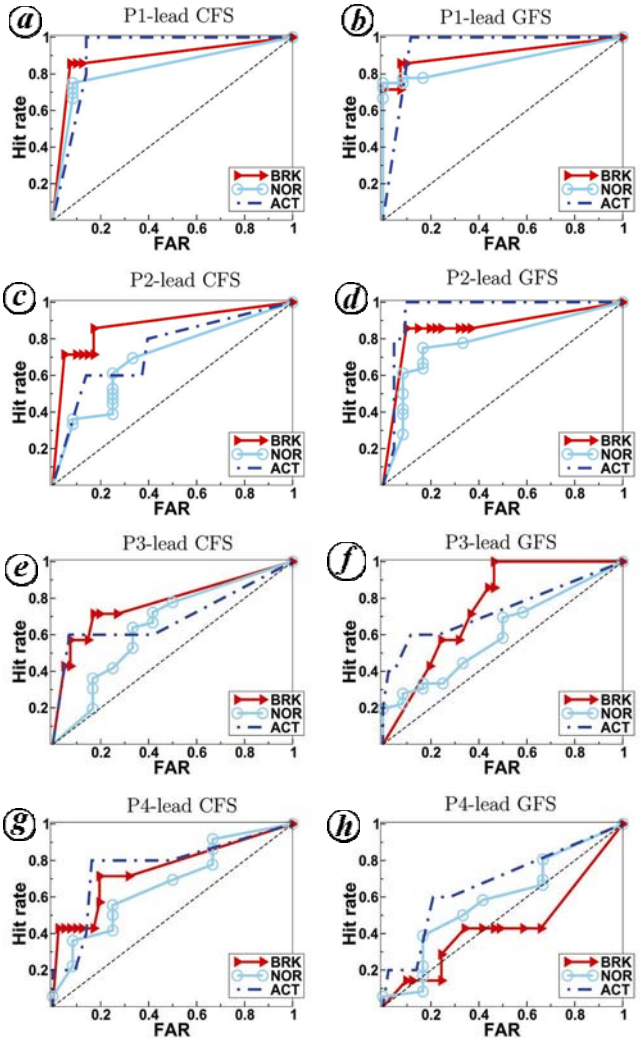

Figure 11. Relative operating characteristic (ROC) curve depicting the hit rate versus false alarm rate of the probibilistic forecast plotted for three categories (break, normal and active). ROC for forecasted lead pentad 1, (***a***) CFS, (***b***) GFS; lead pentad 2, (***c***) CFS, (***d***) GFS; lead pentad 3, (***e***) CFS, (***f***) GFS; lead pentad 4, (***g***) CFS and (***h***) GFS.

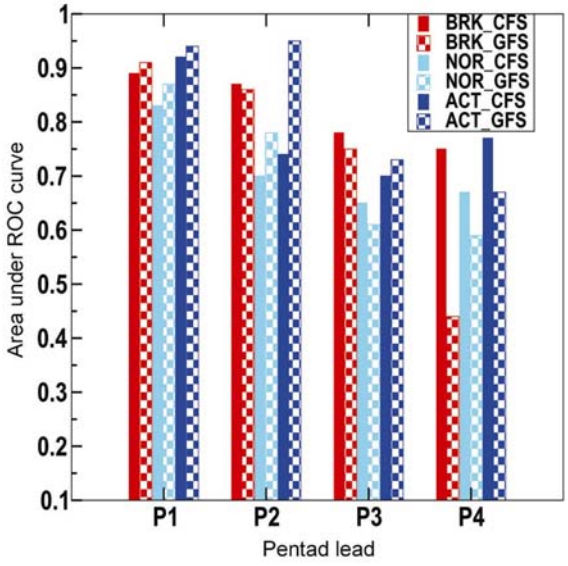

Figure 12. ROC score (area under ROC curve) which provides a summary statistic for the performance of probability forecasts is plotted for three categories forecast for lead pentad 1–4 and for CFS and GFS.

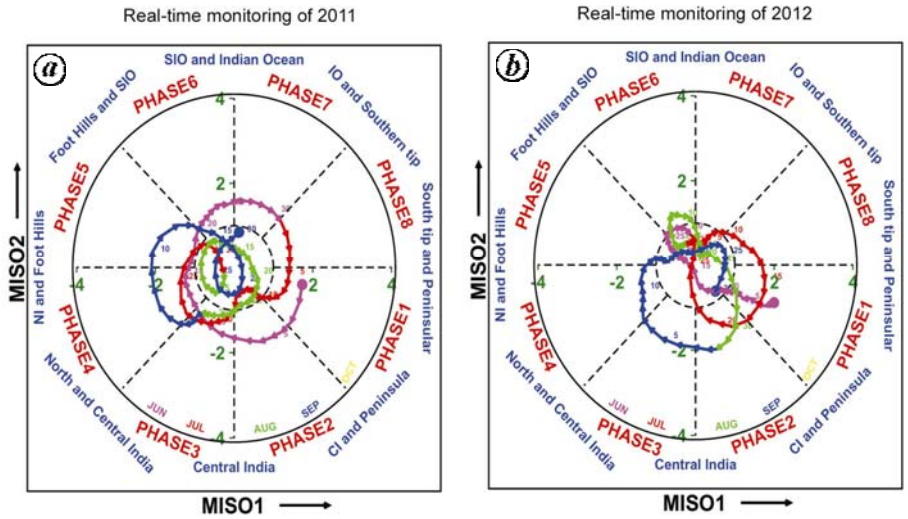

Figure 13. Observed phase diagram (MISO1 and MISO2) during JJAS: (***a***) 2011 and (***b***) 2012.

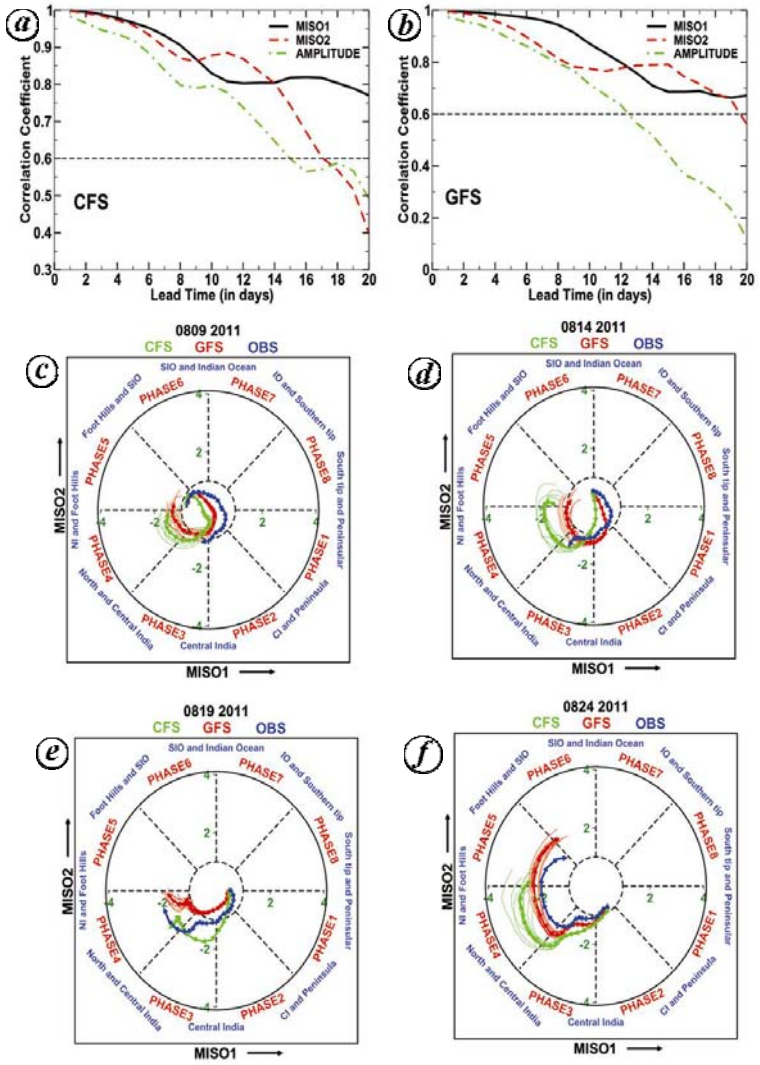

Figure 14. Correlation coefficient for the 18 cases of forecasted MISO indices as a function of lead time for 2011: (***a***) CFS and (***b***) GFS. Phase evolution of an active episode during 25–29 August 2011 for next 20 days from four initial conditions: (***c***) 9 August, (***d***) 14 August, (***e***) 19 August and (***f***) 24 August. Blue line is for observed, red for GFS forecast and green is for CFS forecast.

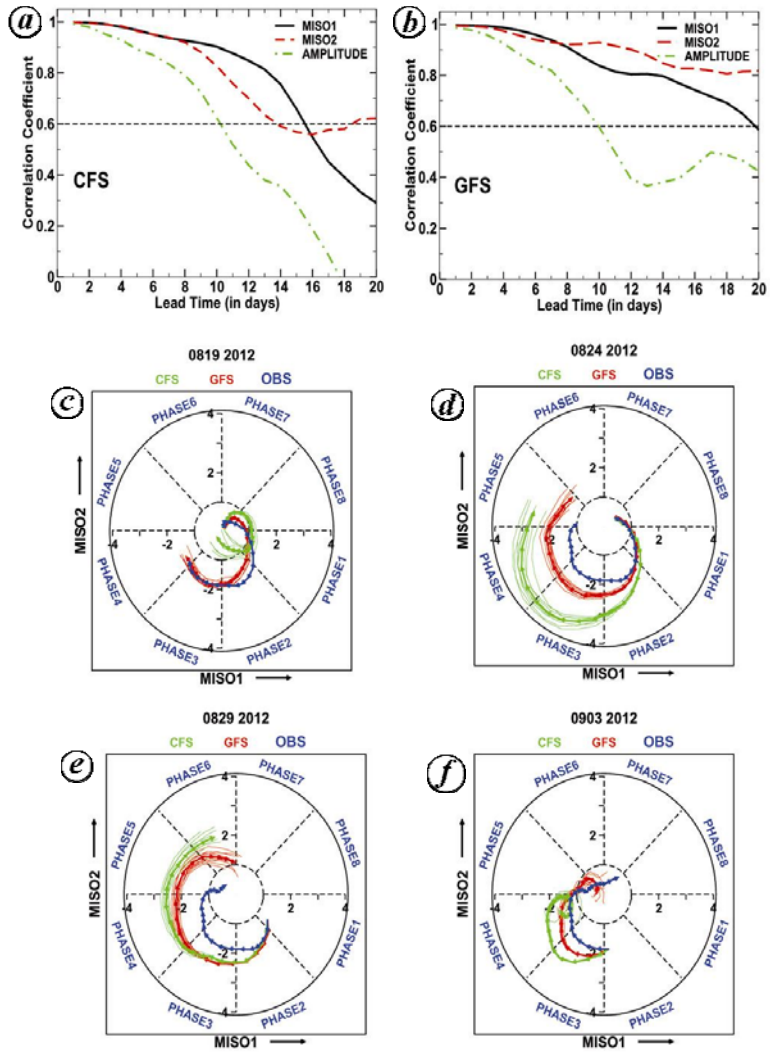

Figure 15. Correlation coefficient for the 18 cases of forecasted MISO indices as a function of lead time for 2012: (***a***) CFS and (***b***) GFS. Phase evolution of an active episode during 4–7 September 2012 for the next 20 days from four initial conditions: (***c***) 19 August, (***d***) 24 August, (***e***) 29 August and (***f***) 3 September. Blue line is for observed OBS, red is for GFS forecast and green is for CFS forecast.

Next, we compared the ERP skill using these two model runs in real-time mode for 2011 and 2012. It is clear that the rainfall prediction skill over the monsoon zone for the CFS is improved in the fourth pentad lead compared to GFS. However, the GFS skill is very much improved in the 5–10 days when forced with bias-corrected SST. The improvement in forecast in CFS in the fourth pentad may be attributed to the realistic simulation in the SST–rainfall relationship. This improvement in the representation of the air–sea interaction is evident from the operational ERP of MISOs as well as the total rainfall for the years 2011 and 2012. The most important improvement is seen in the category-wise forecast in a probabilistic manner. The break and active category is forecasted with better fidelity at the fourth pentad lead. As evident in the AUC, the skill of categorical prediction is higher for GFS in the first two lead pentads. Whereas, categorical prediction skill considerably improved in CFS forecast especially at the fourth pentad lead. The bias-corrected GFS run shows improvement in MISO phase prediction, although MISO amplitude prediction skills in CFS are better or at par with GFS for the two years, 2011 and 2012. More verification runs are required to get realistic scenarios. Although there is a climatological dry bias of rainfall over Indian land in CFS compared to GFS, the MISO amplitudes are over-estimated in CFS run compared to GFS for individual active spell forecasts in the extended range in these two years. This needs more careful examination. There may be large event-to-event variability and prediction skill may also depend on the particular phases of the monsoon circulation. Though sample sizes are limited to two years, considering the general merits and demerits of both models in the extended range, it may be concluded that both coupling and representation of

realistic SST boundary forcing are also important in the ERP applications. However, to establish a definite conclusion, model integrations are being conducted in GFS bias-corrected framework for more years and also in the persisted anomaly framework and will be reported in future.

1. Webster, P. J. and Hoyos, C., Prediction of monsoon rainfall and river discharge on 15–30-day timescales. *Bull. Am. Meteorol. Soc.*, 2004, **85**, 1745–1765.
2. Jones, C., Carvalho, L. M. V., Wayne Higgins, R., Waliser, D. E. and Schemm, J. K. E., A statistical forecast model of tropical intraseasonal convective anomalies. *J. Climate*, 2004, **17**, 2078–2095.
3. Xavier, P. K. and Goswami, B. N., An analog method for realtime forecasting of summer monsoon subseasonal variability. *Mon. Weather Rev.*, 2007, **135**, 4149–4160.
4. Chattopadhyay, R., Sahai, A. K. and Goswami, B. N., Objective identification of nonlinear convectively coupled phases of monsoon intraseasonal oscillation: implications for prediction. *J. Atmos. Sci.*, 2008, **65**, 1549–1569.
5. Dwivedi, S. and Pandey, A. C., Forecasting the Indian summer monsoon intraseasonal oscillations using genetic algorithm and neural network. *Geophys. Res. Lett.*, 2011, **38**, L15801.
6. Waliser, D. E., Lau, K. M., Stern, W. and Jones, C., Potential Predictability of the Madden–Julian oscillation. *Bull. Am. Meteorol. Soc.*, 2003, **84**, 33–50.
7. Waliser, D. E., Stern, W., Schubert, S. and Lau, K. M., Dynamic predictability of intraseasonal variability associated with the Asian summer monsoon. *Q. J. R. Meteorol. Soc.*, 2003, **129**, 2897–2925.
8. Liess, S., Waliser, D. E. and Schubert, S. D., Predictability studies of the intraseasonal oscillation with the ECHAM5 GCM. *J. Atmos. Sci.*, 2005, **62**, 3320–3336.
9. Seo, K.-H., Schemm, J.-K. E., Jones, C. and Moorthi, S., Forecast skill of the tropical intraseasonal oscillation in the NCEP GFS dynamical extended range forecasts. *Climate Dyn.*, 2005, **25**, 265–284.
10. Fu, X., Wang, B., Waliser, D. E. and Tao, L., Impact of atmosphere–ocean coupling on the predictability of monsoon intraseasonal oscillations. *J. Atmos. Sci.*, 2007, **64**, 157–174.
11. Fu, X., Wang, B., Lee, J.-Y., Wang, W. and Gao, L., Sensitivity of dynamical intraseasonal prediction skills to different initial conditions. *Mon. Weather Rev.*, 2011, **139**, 2572–2592.
12. Liu, X., Yang, S., Kumar, A., Weaver, S. and Jiang, X., Diagnostics of subseasonal prediction biases of the Asian summer monsoon by the NCEP climate forecast system. *Climate Dyn.*, 2012; doi: 10.1007/s00382-012-1553-3.
13. Wen, M., Yang, S., Vintzileos, A., Higgins, W. and Zhang, R., Impacts of model resolutions and initial conditions on predictions of the Asian summer monsoon by the NCEP climate forecast system. *Weather Forecast.*, 2012, **27**, 629–646.
14. Goswami, B. N. and Mohan, R. S. A., Intraseasonal oscillations and interannual variability of the Indian summer monsoon. *J. Climate*, 2001, **14**, 1180–1198.
15. Suhas, E., Neena, J. M. and Goswami, B. N., An Indian monsoon intraseasonal oscillations (MISO) index for real time monitoring and forecast verification. *Climate Dyn.*, 2012; doi: 10.1007/s00382-012-1462-5.
16. Goswami, B. N., South Asian monsoon. In *Intraseasonal Variability in the Atmosphere–Ocean Climate System* (eds Lau, W. K. M. and Waliser, D. E.), Springer, 2005, pp. 19–61.
17. Goswami, B. N., Wheeler, M. C., Gottschalck, J. C. and Waliser, D. E., Intra-seasonal variability and forecasting: a review of recent research. In *The Global Monsoon System: Research and Forecast*, World Scientific Publication Company in Collaboration with World Meteorological Organization, 2011, vol. 5, 2nd edn, pp. 389–407.
18. Krishnamurti, T. N., Oosterhof, D. K. and Mehta, A. V., Air–sea interaction on the timescale of 30 to 50 days. *J. Atmos. Sci.*, 1988, **45**, 1304–1322.
19. Woolnough, S. J., Slingo, J. M. and Hoskins, B. J., The relationship between convection and sea surface temperature on intraseasonal timescales. *J. Climate*, 2000, **13**, 2086–2104.
20. Kemball-Cook, S. and Wang, B., Equatorial waves and air–sea interaction in the boreal summer intraseasonal oscillation. *J. Climate*, 2001, **14**, 2923–2942.
21. Slingo, J. M. *et al.*, Intraseasonal oscillations in 15 atmospheric general circulation models: results from an AMIP diagnostic subproject. *Climate Dyn.*, 1996, **12**, 325–357.
22. Wu, M. L. C., Schubert, S., Kang, I. S. and Waliser, D., Forced and free intra-seasonal variability over the South Asian monsoon region simulated by 10 AGCMs. *J. Climate*, 2002, **15**, 2862–2880.
23. Waliser, D. E. *et al.*, AGCM simulations of intraseasonal variability associated with the Asian summer monsoon. *Climate Dyn.*, 2003, **21**, 423–446.
24. Wang, B., Kang, I.-S. and Lee, J. Y., Ensemble simulations of Asian–Australian monsoon variability by 11 AGCMs. *J. Climate*, 2004, **17**, 803–818.
25. Rajendran, K., Nanjundiah, R. S., Gadgil, S. and Srinivasan, J., How good are the simulations of tropical SST-rainfall relationship by IPCC AR4 atmospheric and coupled models? *J. Earth Syst. Sci.*, 2012, **121**, 595–610.
26. Jiang, X., Yang, S., Li, Y., Kumar, A., Liu, X., Zuo, Z. and Jha, B., Seasonal-to-interannual prediction of the Asian summer monsoon in the NCEP climate forecast system Version 2. *J. Climate*, 2012, in press; doi: 10.1175/JCLI-D-12-00437.1.
27. Webster, P. J., Mechanisms of monsoon low-frequency variability: surface hydrological effects. *J. Atmos. Sci.*, 1983, **40**, 2110–2124.
28. Emanuel, K. A., An air–sea interaction model of intraseasonal oscillations in the tropics. *J. Atmos. Sci.*, 1987, **44**, 2324–2340.
29. Kawamura, R., Intraseasonal variability of sea surface temperature over the tropical western Pacific. *J. Meteorol. Soc. Jpn. Ser. II*, 1988, **66**, 1007–1012.
30. Jones, C. and Weare, B. C., The role of low-level moisture convergence and ocean latent heat fluxes in the Madden and Julian oscillation: an observational analysis using ISCCP data and ECMWF analyses. *J. Climate*, 1996, **9**, 3086–3104.
31. Waliser, D. E., Formation and limiting mechanisms for very high sea surface temperature: linking the dynamics and the thermodynamics. *J. Climate*, 1996, **9**, 161–188.
32. Zhang, C., Atmospheric intraseasonal variability at the surface in the tropical western Pacific Ocean. *J. Atmos. Sci.*, 1996, **53**, 739–758.
33. Hendon, H. H. and Glick, J., Intraseasonal air–sea interaction in the tropical Indian and Pacific Oceans. *J. Climate*, 1997, **10**, 647–661.
34. Lau, K. and Sui, C., Mechanisms of short-term sea surface temperature regulation: observations during {TOGA} {COARE}. *J. Climate*, 1997, **10**, 465–472.
35. Sperber, K. R., Slingo, J. M., Inness, P. M. and Lau, W. K.-M., On the maintenance and initiation of the intraseasonal oscillation in the NCEP/NCAR reanalysis and in the GLA and UKMO AMIP simulations. *Climate Dyn.*, 1997, **13**, 769–795.
36. Jones, C., Waliser, D. E. and Gautier, C., The influence of the Madden–Julian oscillation on ocean surface heat fluxes and sea surface temperature. *J. Climate*, 1998, **11**, 1057–1072.
37. Fu, X., Wang, B., Li, T. and McCreary, J. P., Coupling between northward-propagating, intraseasonal oscillations and sea surface temperature in the Indian Ocean. *J. Atmos. Sci.*, 2003, **60**, 1733–1753.
38. Fu, X. and Wang, B., The boreal-summer intraseasonal oscillations simulated in a hybrid coupled atmosphere–ocean model. *Mon. Weather Rev.*, 2004, **132**, 2628–2649.

39. Zheng, Y., Waliser, D. E., Stern, W. F. and Jones, C., The role of coupled sea surface temperatures in the simulation of the tropical intraseasonal oscillation. *J. Climate*, 2004, **17**, 4109–4134.
40. Fu, X., Wang, B., Waliser, D. E. and Tao, L., Impact of atmosphere–Ocean coupling on the predictability of monsoon intraseasonal oscillations. *J. Atmos. Sci.*, 2007, **64**, 157–174.
41. Sengupta, D., Goswami, B. N. and Senan, R., Coherent intraseasonal oscillations of ocean and atmosphere during the Asian summer monsoon. *Geophys. Res. Lett.*, 2001, **28**, 4127–4130.
42. Vecchi, G. A. and Harrison, D. E., Monsoon breaks and subseasonal sea surface temperature variability in the Bay of Bengal. *J. Climate*, 2002, **15**, 1485–1493.
43. Wang, B., Webster, P., Kikuchi, K., Yasunari, T. and Qi, Y., Boreal summer quasi-monthly oscillation in the global tropics. *Climate Dyn.*, 2006, **27**, 661–675.
44. Roxy, M. and Tanimoto, Y., Role of SST over the Indian Ocean in influencing the intraseasonal variability of the Indian summer monsoon. *J. Meteorol. Soc. Jpn.*, 2007, **85**, 349–358.
45. Wang, B. *et al.*, Fundamental challenge in simulation and prediction of summer monsoon rainfall. *Geophys. Res. Lett.*, 2005, **32**, L15711.
46. Seo, K.-H., Schemm, J.-K. E., Wang, W. and Kumar, A., The boreal summer intraseasonal oscillation simulated in the NCEP climate forecast system: the effect of sea surface temperature. *Mon. Weather Rev.*, 2007, **135**, 1807–1827.
47. Pegion, K. and Kirtman, B. P., The impact of air–sea interactions on the sim1ulation of tropical intraseasonal variability. *J. Climate*, 2008, **21**, 6616–6635.
48. Bellon, G., Sobel, A. H. and Vialard, J., Ocean–atmosphere coupling in the monsoon intraseasonal oscillation: a simple model study. *J. Climate*, 2008, **21**, 5254–5270.
49. Sud, Y. C., Walker, G. K., Zhou, Y. P. and Lau, W. K.-M., Influence of local and remote sea surface temperatures on precipitation as inferred from changes in boundary-layer moisture convergence and moist thermodynamics over global oceans. *Q. J. R. Meteorol. Soc.*, 2008, **134**, 147–163.
50. Krishnamurthy, V. and Kirtman, B. P., Relation between Indian monsoon variability and SST. *J. Climate*, 2009, **22**, 4437–4458.
51. Roxy, M. and Tanimoto, Y., Influence of sea surface temperature on the intraseasonal variability of the South China Sea summer monsoon. *Climate Dyn.*, 2012, **39**, 1209–1218.
52. Flatau, M., Flatau, P. J., Phoebus, P. and Niiler, P. P., The feedback between equatorial convection and local radiative and evaporative processes: the implications for intraseasonal oscillations. *J. Atmos. Sci.*, 1997, **54**, 2373–2386.
53. Waliser, D. E., Lau, K. M. and Kim, J.-H., The influence of coupled sea surface temperatures on the Madden–Julian oscillation: a model perturbation experiment. *J. Atmos. Sci.*, 1999, **56**, 333–358.
54. Inness, P. M., Slingo, J. M., Guilyardi, E. and Cole, J., Simulation of the Madden–Julian oscillation in a coupled general circulation model. Part II: the role of the basic state. *J. Climate*, 2003, **16**, 365–382.
55. Sperber, K. R., Madden–Julian variability in NCAR CAM2.0 and CCSM2.0. *Climate Dyn.*, 2004, **23**, 259–278.
56. Saha, S. *et al.*, The NCEP climate forecast system. *J. Climate*, 2006, **19**, 3483–3517.
57. Saha, S. *et al.*, The NCEP climate forecast system reanalysis. *Bull. Am. Meteorol. Soc.*, 2010, **91**, 1015–1057.
58. Griffies, S., Matthew, M., Harrison, J., Pacanowski, R. C. and Rosati, A., A technical guide to OM4, GFDL Ocean Group Technical Report No. 5, NOAA/Geophysical Fluid Dynamics Laboratory, Princeton, NJ, USA, 2004, p. 342.
59. Abhilash, S. *et al*., Performance of an ensemble prediction system based on CFSv2 for the extended range prediction of active–break spells of Indian summer monsoon rainfall during 2011. IITM Research Report, 2012.
60. Huffman, G. J. *et al.*, Global precipitation at one-degree daily resolution from multisatellite observations. *J. Hydrometeorol.*, 2001, **2**, 36–50.
61. Adler, R. F. *et al*., The version-2 Global Precipitation Climatology Project (GPCP) monthly precipitation analysis (1979–present). *J. Hydrometeorol.*, 2003, **4**, 1147–1167.
62. Rajeevan, M., Pai, D. S., Anil Kumar, R. and Lal, B., New statistical models for long-range forecasting of southwest monsoon rainfall over India. *Climate Dyn.*, 2006, **28**, 813–828.
63. Mitra, A. K., Bohra, A. K., Rajeevan, M. N. and Krishnamurti, T. N., Daily Indian precipitation analysis formed from a merge of rain–gauge data with the TRMM TMPA satellite-derived rainfall estimates. *J. Meteorol. Soc. Jpn. A*, 2009, **87**, 265–279.
64. Kalnay, E. *et al*., The NCEP/NCAR 40-year reanalysis project. *Bull. Am. Meteorol. Soc.*, 1996, **77**, 437–471.
65. Roxy, M., Tanimoto, Y., Preethi, B., Terray, P. and Krishnan, R., Intraseasonal SST–precipitation relationship and its spatial variability over the tropical summer monsoon region. *Climate Dyn.*, 2012, doi: 10.1007/s00382-012-1547-1.
66. Sahai, A. K., Chattopadhyay, R. and Goswami, B. N., A SST based large multi-model ensemble forecasting system for Indian summer monsoon rainfall. *Geophys. Res. Lett.*, 2008, **35**, L19705, doi: 10.1029/2008GL035461.
67. Carreras, B. A., Newman, D. E., van Milligen, B. P. and Hidalgo, C., Long-range time dependence in the cross-correlation function. *Phys. Plasmas*, 1999, **6**, 485–494.
68. Zhou, W. X., Multifractal detrended cross-correlation analysis for two nonstationary signals. arXiv:0803.2773, 2008, **77**, doi: 10.1103/PhysRevE.77.066211.
69. Zhu, X., Fraedrich, K., Liu, Z. and Blender, R., A demonstration of long-term memory and climate predictability. *J. Climate*, 2010, **23**, 5021–5029.

ACKNOWLEDGEMENTS. The Indian Institute of Tropical Meteorology (IITM), Pune is fully funded by the Ministry of Earth Sciences (MoES), New Delhi. We thank Prof. B. N. Goswami, Director, IITM for encouragement and support to pursue this study; we thank NCEP for reanalysis datasets and for transferring the CFS system under the MoU between MoES and NOAA. We also thank IMD and GPCP for daily rainfall data. S.S. thanks the Council of Scientific and Industrial Research, New Delhi, for a research fellowship. Use of the software GRACE, NCL (NCAR) and GrADS (COLA) is acknowledged. The constructive comments by two anonymous reviewers helped to improve the manuscript.